

Hydrothermal synthesis of Mg-doped LiMn_2O_4 spinel cathode materials with high cycling performance for lithium-ion batteries

Fenglan Luo^{1,2}, Hongyan Xie^{1,2,3,*}, Huixin Jin^{1,2}, Yelin Han^{1,2}

¹ College of Material and Metallurgy, Guizhou University, Guiyang, 550025, China.

² Guizhou Province Key Laboratory of Metallurgical Engineering and process Energy Saving, Guiyang, 550025, China.

³ State Key Laboratory of Pressure Hydrometallurgical Technology of Associated Nonferrous Metal Resources, Yunnan, Kunming, 650503, China.

* E-mail: hyxie@gzu.edu.cn

Received: 27 February 2022 / Accepted: 28 March 2022 / Published: 7 May 2022

Spinel $\text{LiMg}_x\text{Mn}_{2-x}\text{O}_4$ cathode materials were synthesised using a hydrothermal method, with the effects of doping Mg on the structure and electrochemical performance of LiMn_2O_4 subsequently investigated. It was found that no other hybrid phases existed in the $\text{LiMg}_x\text{Mn}_{2-x}\text{O}_4$ and that doped Mg cannot change the spinel lattice type of LiMn_2O_4 . An appropriate Mg content was beneficial for improving the crystallinity and particle uniformity of the samples. The electrochemical performance of the $\text{LiMg}_x\text{Mn}_{2-x}\text{O}_4$ was assessed in the 2.9~4.3 V range, with the specific discharge capacity of the LiMn_2O_4 potentially reaching 139.9 mAh g^{-1} at 0.2 C, with a capacity retention rate of 63.76% after 100 cycles. Furthermore, the $\text{LiMn}_{1.97}\text{Mg}_{0.03}\text{O}_4$ demonstrated an excellent cycling performance at both room temperature (25°C) and at a high temperature (55°C). At 25°C, the first specific discharge capacity was 124.3 mAh g^{-1} at 0.2 C, with a capacity retention rate of 94.29% after 100 cycles, while the specific discharge capacity can reach 94.8 mAh g^{-1} at 5 C and 74.0 mAh g^{-1} at 10 C. At 55°C, the initial specific discharge capacity was 125.6 mAh g^{-1} at 0.2 C, with a capacity retention rate of 85.43% after 100 cycles. The cyclic voltammogram curves and electrochemical impedance spectroscopy results indicated that, compared with the pristine LiMn_2O_4 , the $\text{LiMn}_{1.97}\text{Mg}_{0.03}\text{O}_4$ had a larger Li^+ -ion diffusion coefficient and smaller resistance during the charge–discharge process. Overall, the results indicated that Mg doping is beneficial in improving the electrochemical performance of spinel LiMn_2O_4 .

Keywords: Lithium ion batteries, Spinel LiMn_2O_4 , Mg doping, Hydrothermal method, High cycling performance

1. INTRODUCTION

Currently, due to the rapid development of the economy, the world is faced with a series of issues, including resource shortage, energy exhaustion and environmental deterioration. These issues have seriously threatened the survival and development of human beings, forcing us to seek the development of green renewable energy. Worldwide, countries have made great efforts to research and utilise renewable and green energy sources, such as solar energy, wind energy and tidal energy. However, these sources are surrounded by uncertainty in terms of both time and space [1–4], with the development of cheap and environmentally friendly energy storage technology becoming the key factor in utilising such energy sources. Lithium-ion batteries have the advantages of small size, high voltage, large capacity, long life and no memory effect [5, 6] and are thus regarded as an ideal means of energy storage and conversion, currently widely used in the fields of electronics, communications and power vehicles [7]. Spinel LiMn_2O_4 with a three-dimensional lithium (Li)-ion diffusion channel is deemed to be an excellent cathode material [8–10], with the material having considerable research value and development potential due to the attendant high-voltage platform, abundant manganese (Mn) resources, low production cost, good safety and environment friendly characteristics [11–13].

However, spinel LiMn_2O_4 exhibits serious capacity fading during the charge–discharge process due to the Jahn–Teller distortion effect, the dissolution of the Mn and the oxygen defect, which is hindering the material’s commercial development [14, 15]. The Jahn–Teller distortion results in the transformation of the LiMn_2O_4 from a cubic crystal phase to a tetragonal crystal phase [16–19], which is accompanied by both volume change and lattice strain, making the reversibility of Li^+ insertion and extraction difficult [20]. A portion of the Mn ions enter the tetrahedron 8a position and the Li ions enter the tetrahedron 16c position, resulting in cation mixing and irreversible capacity. Meanwhile, the dissolution of the Mn is due to the disproportionation reaction of Mn^{3+} ions, $\text{Mn}^{3+} \rightarrow \text{Mn}^{2+} + \text{Mn}^{4+}$, with the resulting Mn^{2+} easily soluble in the electrolyte solution [21–23]. In addition, the hydrofluoric acid in the electrolyte can corrode the cathode material, resulting in the dissolution of the Mn [24]. Meanwhile, hypoxic LiMn_2O_4 emerges due to the effect of poor synthesis conditions, such as an excessive synthesis temperature or insufficient oxygen [25, 26]. Doping ions presents one of the effective methods for alleviating the capacity decay, with numerous studies demonstrating that partially replacing the Mn^{3+} with doping cations, such as Ni^{2+} , Co^{3+} , Al^{3+} , Cr^{3+} , Mg^{2+} , and Fe^{3+} , can inhibit the Jahn–Teller distortion, thus enhancing the structural stability of spinel LiMn_2O_4 [27–32].

In this paper, $\text{LiMg}_x\text{Mn}_{2-x}\text{O}_4$ was synthesised using a hydrothermal method, with the effect of doping Mg^{2+} ions on the crystal structure of the material subsequently studied along with the discharge capacity, cycling performance and Li^+ -ion diffusion behaviour of the $\text{LiMg}_x\text{Mn}_{2-x}\text{O}_4$ cathode materials.

2. EXPERIMENTAL

2.1 Synthesis of materials

Various $\text{LiMg}_x\text{Mn}_{2-x}\text{O}_4$ ($x = 0, 0.01, 0.02, 0.03, 0.04, 0.05$) samples were synthesised using the hydrothermal method. Here, 0.79 g of KMnO_4 and 0.21 g of $\text{LiOH}\cdot\text{H}_2\text{O}$ were dissolved in 50 mL of

deionised water before the corresponding amount of MgO was added along with an appropriate amount of aniline (the aniline/KMnO₄ molar ratio = 0.2) to serve as the reducing agent. The solution was then stirred evenly for 20 min and transferred to a 100-mL reactor for 12 h, with the reaction temperature set to 200°C. The resulting mixture was then filtered and dried before heat treatment at 600°C was performed for 3 h in a high-temperature tube furnace to stabilise the crystal pattern and obtain the LiMg_xMn_{2-x}O₄ (x = 0, 0.01, 0.02, 0.03, 0.04, 0.05) samples, with the corresponding samples labelled LMO, LMMO-1, LMMO-2, LMMO-3, LMMO-4 and LMMO-5.

2.2 Materials characterization

An X-ray diffractometer (XRD, D/Max2500, Japan) was used to characterise the crystal structure and conduct the phase analysis of the samples. Here, the radiation source was Cu-K α , the wavelength was 0.15406 nm, the scanning rate was 4°min⁻¹ and the scanning range was 10°–80°. Meanwhile, scanning electron microscopy (SEM, Zeiss Sigma300, Germany) was used to observe the morphology of the samples, while energy dispersive spectroscopy (EDS) was used for the elemental analysis. Finally, X-ray photoelectron spectroscopy (XPS, ThermoFisher, Thermo Scientific K-Alpha+) was adopted to evaluate the valence state of the Mg-doped LiMn₂O₄ nanoparticles.

2.3 Electrochemical characterization

Acetylene black, polyvinylidene fluoride and LiMn_{2-x}Ti_xO₄ were mixed in an agate mortar with a mass ratio of 8:1:1 before an appropriate amount of N-methylpyrrolidone was added. After being uniformly ground, the slurry was evenly spread onto aluminium foil and dried. Following this, a hole punch was used to prepare a positive electrode sheet with a diameter of 11 mm, while a Li sheet and microporous polypropylene film (Celgard 2400) were used for the negative electrode and the separator, respectively. Finally, 1 M LiPF₆ in a mixture of ethylene carbonate (EC), dimethyl carbonate (DMC) and diethyl carbonate (DEC) (V_{EC}:V_{DMC}:V_{DEC} = 1:1:1) was used as the solution electrolyte. The cells were assembled into button batteries and placed in a glove box.

A battery test system (LAND-CT2001A, Wuhan, China) was used to conduct a constant current charge/discharge experiment on the prepared half-cell at room temperature (25°C), with the cut-off potential of the charge/discharge set between 2.9 and 4.3 V. Cyclic voltammogram curves (CVs) were then obtained using an electrochemical workstation (CHI600A), which was also used to obtain the electrochemical impedance spectroscopy (EIS) spectra. Here, the frequency range was 0.01 Hz–10 kHz, while the amplitude was 5 mV.

3. RESULTS AND DISCUSSION

3.1 Structure and morphology

The XRD patterns of all the samples are shown in Fig. 1. The characteristic diffraction peaks, (111), (311), (222), (400), (331), (511), (440) and (531), of LiMn₂O₄ appeared across all the samples,

with the peaks observed to be sharp. No impurity peaks were detected, indicating that the hydrothermal method used in this study was effective in synthesising the pure phase of the spinel LMO with fine crystallisation products. The enlarged (400) diffraction peak in the range of 43.5° – 45° can be seen in the right side of Fig. 1. Here, with the increase in doping amount, the lattice of the LiMn_2O_4 contracted and the (400) diffraction peak shifted towards a larger angle.

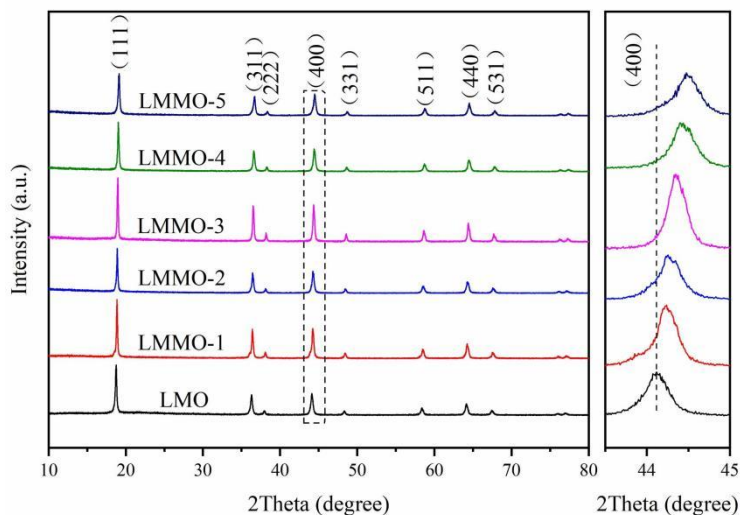


Figure 1. The XRD patterns of the samples and the enlarged (400) diffraction peak

Table 1. Lattice parameters of the samples

Samples	Lattice parameters		$I_{(311)}/I_{(400)}$	$\text{FWHM}_{(400)}$
	a (Å)	V (Å ³)		
LMO	8.2249	556.4178	0.9409	0.3295
LMMO-1	8.2238	556.1912	0.9908	0.2735
LMMO-2	8.2207	555.5523	0.9884	0.2930
LMMO-3	8.2174	554.8814	0.9961	0.2601
LMMO-4	8.2154	554.4738	0.9928	0.3461
LMMO-5	8.2143	554.2623	0.9926	0.3266

The lattice parameters of the samples were obtained via Rietveld refinement of the XRD data (Table 1). The crystal structure, $Fd\bar{3}m$, was used in these refinements, while the lattice constants $a = 8.2249, 8.2238, 8.2174, 8.2154$ and 8.2143 Å were used for LMMO-1, LMMO-2, LMMO-3, LMMO-4 and LMMO-5, respectively. The lattice parameters gradually decreased with the increase in Mg content (x). The radius of the Mg^{2+} ions (0.065 Å) was similar to that of the substituted ion Mn^{3+} ions (0.0645 Å), while the Mg–O bonding energy was higher than the Mn–O bonding energy [33, 34], a situation that

led to the lattice shrinkage of the doped samples, implying enhanced binding forces between the structural atoms within the spinel, reduced crystal cell volume and an enhanced structural stability of the product. The (311)/(400) intensity ratios and the full width at half maximum (FWHM) values of (400) are also listed in Table 1. Compared with the LMO, the Mg-doped samples exhibited higher (311)/(400) intensity ratios and smaller half peak widths, indicating that the structural stability of the Mg-doped samples was improved, especially in the case of the LMMO-3 sample. Furthermore, previous research results [35, 36], which have good crystallinity and electrochemical properties.

The SEM images of $\text{LiMg}_x\text{Mn}_{2-x}\text{O}_4$ (Fig. 2) revealed that the crystal sizes of the samples were small and submicron, while the particles were octahedral or polyhedral in shape, indicating that the doping of the Mg^{2+} ions did not change the morphology of the materials. Compared with the particles of the undoped LiMn_2O_4 , those of the $\text{LiMg}_x\text{Mn}_{2-x}\text{O}_4$ were more regular, while the crystal size was slightly decreased. Here, it can be inferred that a high Mg doping ratio results in a decrease in the single crystal size, which is essentially in line with the above analysis. Meanwhile, Fig. 3 presents the EDS spectrum and the element mapping of the LMMO-3, from which the elemental composition of the sample could be recorded. Here, Mn, O and Mg elements were observed in the sample, confirming the successful doping of the Mg^{2+} ions.

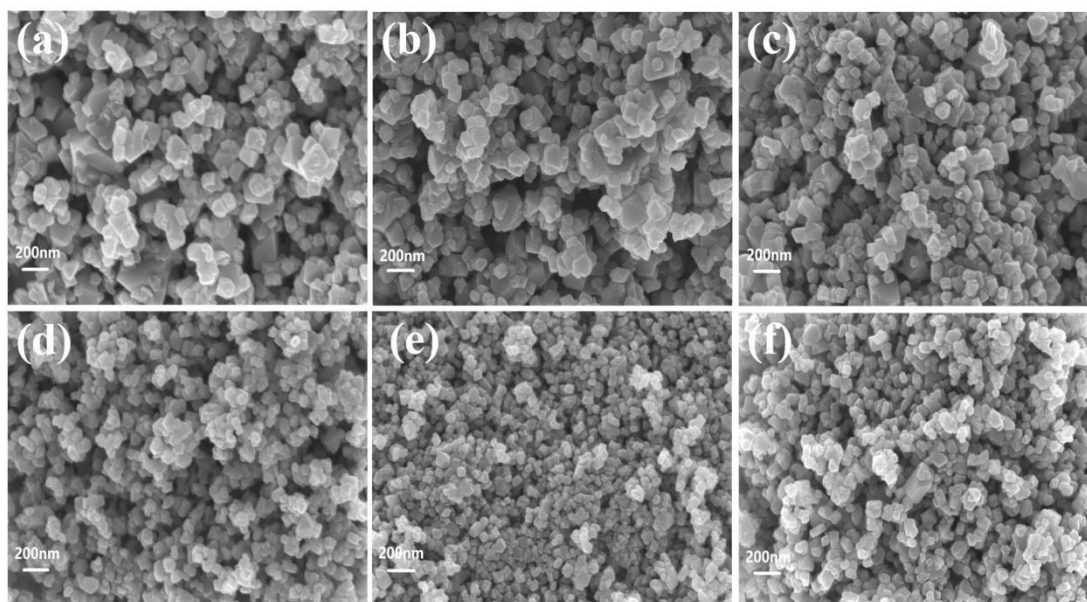


Figure 2. The SEM images of the samples: (a) LMO, (b) LMMO-1, (c) LMMO-2, (d) LMMO-3, (e) LMMO-4 and (f) LMMO-5

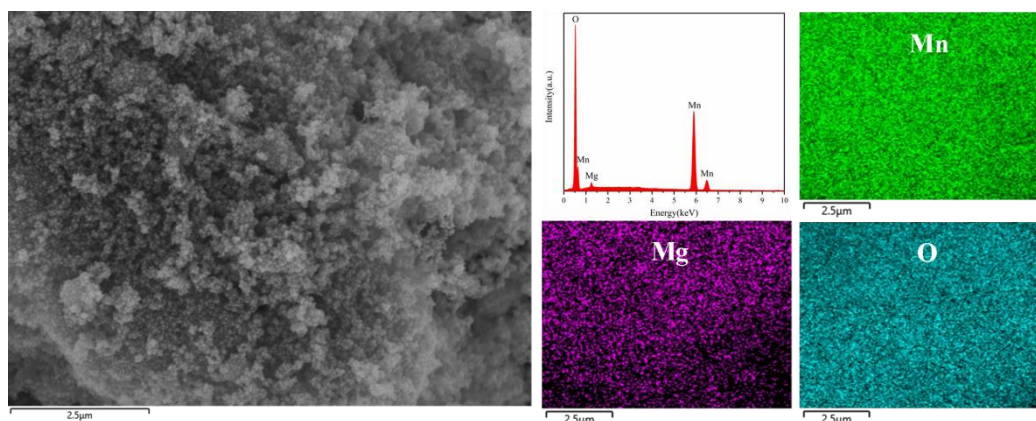


Figure 3. The EDS mapping of the LMMO-3 sample

The XPS spectra of the LMO and LMMO-3 samples are shown in Fig. 4a, while the full range of the XPS spectra is presented in the remainder of the figure. Here, the characteristic peaks of C1s, O1s, Mn2p and Mg1s were clearly observable in the LMMO-3 sample.

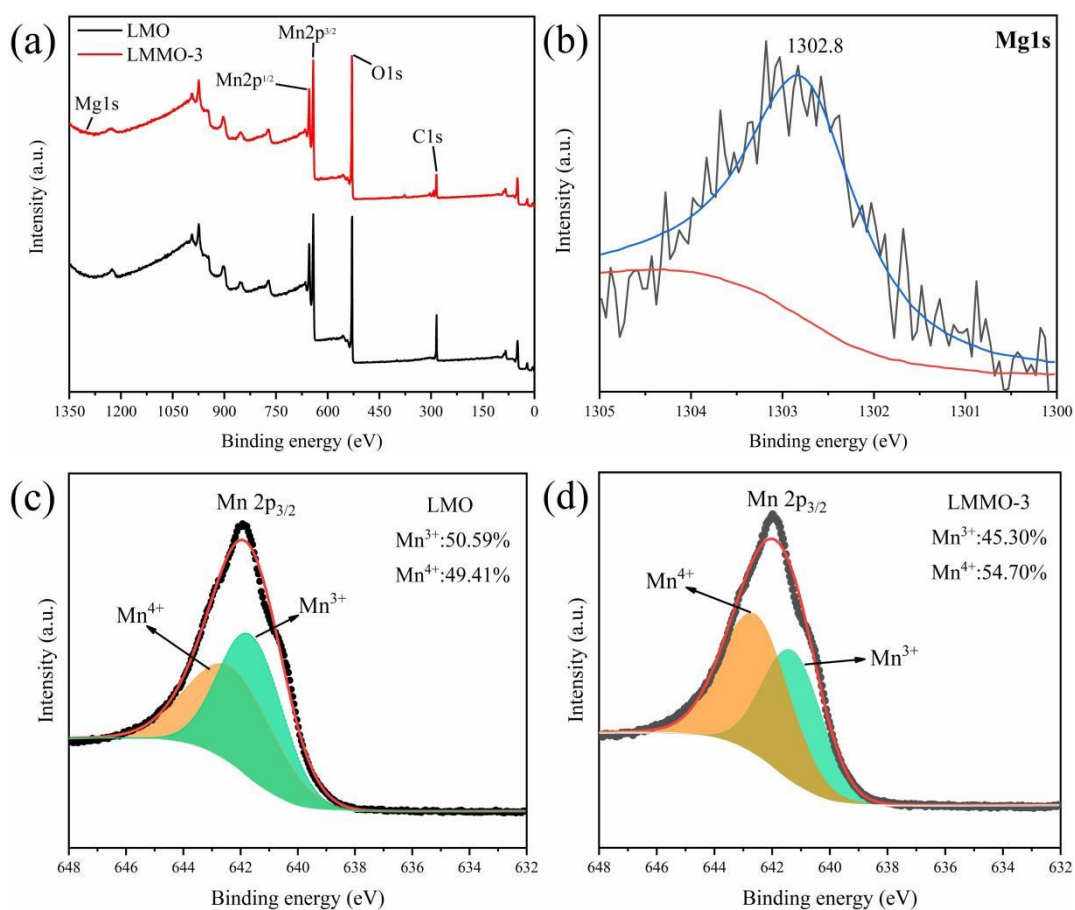


Figure 4. (a) The XPS full spectra of the LMO and LMMO-3 samples, (b) the Mg1s peaks of the LMO-3, (c) the fitted Mn 2p_{3/2} peaks of the LMO and (d) the fitted Mn 2p_{3/2} peaks of the LMMO-3

The XPS peak at the binding energy of 1302.8 eV, as is shown in Fig. 4b, was attributed to Mg1s, indicating that the Mg ions were doped into the lithium manganate lattice. As is shown in Fig. 4c, the representative peak at the bond energy of 642.14 eV corresponded to Mn2p_{3/2}, indicating that in the lithium manganate lattice, Mn ions mainly coexisted with Mn³⁺ and Mn⁴⁺ ions, which were around 641.5 and 642.6 eV, respectively [37]. Based on the different photoelectron peak-area ratios, the percentage of Mn³⁺/Mn⁴⁺ of the LMO sample was 50.59%/49.41%. As is shown in Fig. 4d, the Mg²⁺-ion doping reduced the percentage of Mn³⁺/Mn⁴⁺ (45.30% /54.70%), indicating that Mg²⁺ replaced the Mn³⁺ sites in the crystal structure of the material. It was also found that the Mn⁴⁺ content increased to a certain extent (54.70%), potentially alleviating the Jahn–Teller effect and improving the structural stability of the LiMn₂O₄ cathode material [38].

3.2 Electrochemical performance

A galvanostatic charge/discharge test was conducted at a range of 2.9–4.3 V, with the results shown in Fig. 5. Here, Fig. 5a shows the first charge/discharge curves of all the samples at 0.2 C. The samples exhibited two charging and discharging platforms at around 3.95 and 4.10 V, which indicated that in the LMMO with a low Mg doping ratio, the Li extraction–insertion process was similar to the pure-phase LMO. All the samples underwent two reversible redox processes. Note that the LMO had a high first specific discharge capacity of 139.9 mAh g⁻¹, while with the increase in doping content, the initial specific discharge capacities of the samples tended to decrease (127.1, 122.2, 124.3, 111.4 and 105.9 mAh g⁻¹, respectively). This was because Li⁺ (0.0076 Å) and Mg²⁺ (0.0065 Å) have similar ion radii and Mg-materials are prone to Mg²⁺ migration to Li⁺ holes, resulting in structural disorder, meaning Mg doping will have an effect on the specific capacity of the material [39]. However, the cycle performance curves at 0.2 C (Fig. 5b) indicated that the undoped LiMn₂O₄ underwent rapid capacity fade, with its specific discharge capacity 89.2 mAh g⁻¹ and its capacity retention 63.76% after 100 cycles. With the increase in Mg doping quantity, there initially emerged an increasing trend of the capacity retention before a subsequent decrease. The discharge specific capacities of the samples, from LMMO-1 to LMMO-5, were 109.6, 107.6, 117.2, 103.1 and 99.1 mAh g⁻¹, respectively, with capacity retentions of 86.23%, 88.05%, 94.29%, 92.55% and 93.58%, respectively, after 100 cycles. Among all the samples, LMMO-3 exhibited a higher initial discharge capacity and the best cycling retention, suggesting that the Mg doping of LiMn₂O₄ can indeed improve the cyclic stability of the material. The rate capabilities of the samples at various current rates are shown in Fig. 5c. Here, it was clear that all the doped samples had a higher capacity than the undoped LiMn₂O₄ at a high current density. Specifically, the discharge capacities of LMMO-3 were 124.5, 126.1, 120.7, 94.8 and 74.0 mAh g⁻¹ at 0.2, 0.5, 1, 5 and 10 C, respectively, the best performance among all the samples. Furthermore, the rate performance of the Mg-doped LiMn₂O₄ was far better than that of the LiMn₂O₄ prepared via hydrothermal synthesis reported by Lv et al. [40], again indicating that Mg doping can improve the electrical conductivity and Li⁺ diffusion behaviour of the material.

Table 2 shows the relevant electrochemical data of the LiMn₂O₄ cathode material prepared by doping different metal ions in previous studies. Here, it was found that the addition of a specific amount

of ion doping will reduce the capacity of the cathode material but will assist in maintaining the stability of the cycle properties. In the present work, the Mg-doped LiMn_2O_4 spinel cathode materials prepared via hydrothermal synthesis demonstrated an excellent electrochemical performance, with a high initial discharge ratio capacity and stable cycle performance.

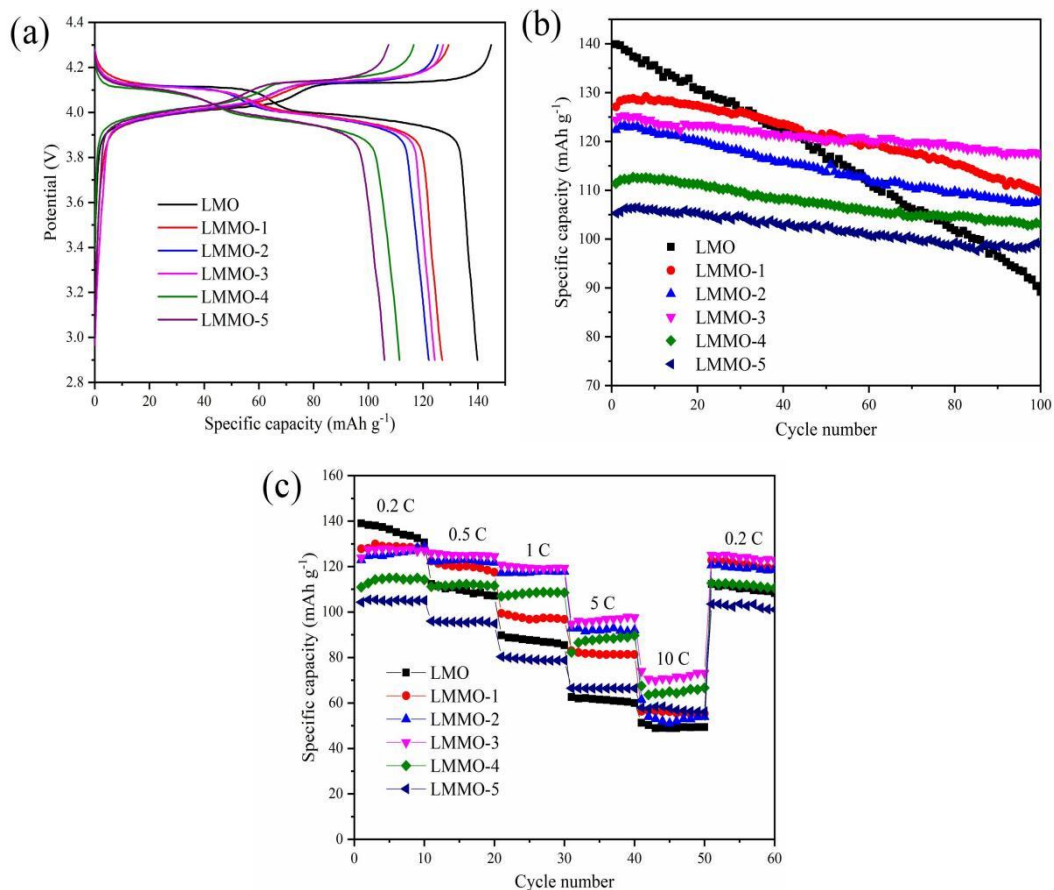


Figure 5. Galvanostatic charge/discharge test results for the samples between 3.0 and 4.5 V at room temperature: (a) initial charge/discharge curves at 0.2 C, (b) cycling performances at 0.2 C and (c) rate performances at various current densities

Table 2. Performance parameters of the LiMn_2O_4 synthesised by doping different metal ions

Methods	Initial discharge capacity(mAh g^{-1})	Dicharge rate/number of cycles	Capacity retention	Reference
Mg-doped	124.3	100cycles at 0.2C	94.29%	This work
Al-doped	100.7	400cycles at 0.5C	93.5%	[41]
Sc-doped	117	500cycles at 1C	74.0%	[42]
Ni-doped	105.0	1000cycles at 1C	68.6%	[47]
Co-doped(Mg-Si)	128.3	100cycles at 0.5C	92.8%	[36]
Co-doped(Ni-Mg)	112.3	1000cycles at 1C	73.7%	[46]
Co-doped(Al-Si-Mg)	123.6/55°C	100cycles at 0.5C	93.8%/55°C	[49]

Compared with the electrochemical performance at 25°C, the capacity decay of spinel LiMn_2O_4 materials tends to be more severe at high temperatures (55°C) [43]. The cycling performance curves of the LMO and LMMO-3 at 0.2 C and 55°C are shown in Fig. 6. Here, the sample doped with Mg^{2+} had a lower initial specific discharge capacity, which was due to the partial substitution of the Mn^{3+} with Mg^{2+} , while the initial specific discharge capacity of the LMO was 128.6 mAh g^{-1} . However, after 100 cycles, the discharge capacity decayed to 61.6 mAh g^{-1} , while the capacity retention was only 44.48%. The initial specific discharge capacity of the LMMO-3 at 55°C was 125.6 mAh g^{-1} , with capacity retention of 85.43% after 100 cycles. These results were superior to those reported by Cai et al. under similar conditions (50 cycles, 82%/55°C) [41], confirming that 3% Mg doping can greatly improve the high-temperature stability of spinel LiMn_2O_4 [44], while the Jahn–Teller distortion effect can also be effectively alleviated.

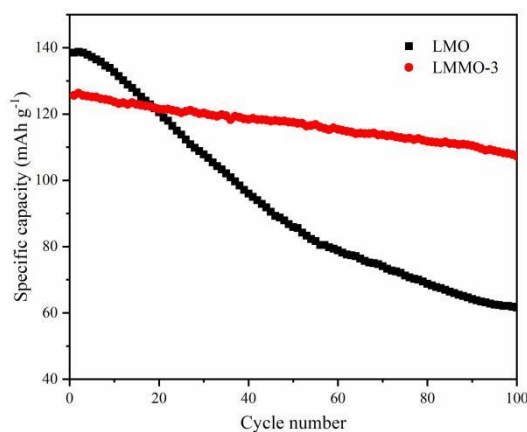


Figure 6. Cycling performances of the LMO and LMMO-3 at 0.2 C at a high temperature (55°C)

The cyclic voltammetry curves of the initial five cycles of the LMO and LMMO-3 at a scanning rate of 0.02 mV s^{-1} are shown in Fig. 7. Here, it was clear that the CV curves of the LMO and LMMO-3 were similar in shape, with two pairs of reversible redox peaks corresponding to the two-step Li^+ intercalation/deintercalation process of LiMn_2O_4 . Compared with the CV curves of the LMO and LMMO-3, the redox peaks of the LMMO-3 exhibited better symmetry, indicating that the Li^+ extraction and insertion process demonstrated improved reversibility. The coincidence of the CV curves with different cycles reflects the cycle stability of the materials. As Fig. 7a shows, with the increase in cycle number, the redox potential difference of the LMO samples gradually increased, while the corresponding peak current significantly decreased. The overlap of the initial five CV curves was clearly poor. Meanwhile, as is shown in Fig. 7b, the initial five cycles of the LMMO-3 completely overlapped, indicating that the structure will be more stable and less prone to distortion during the process of Li -ion extraction/insertion [45].

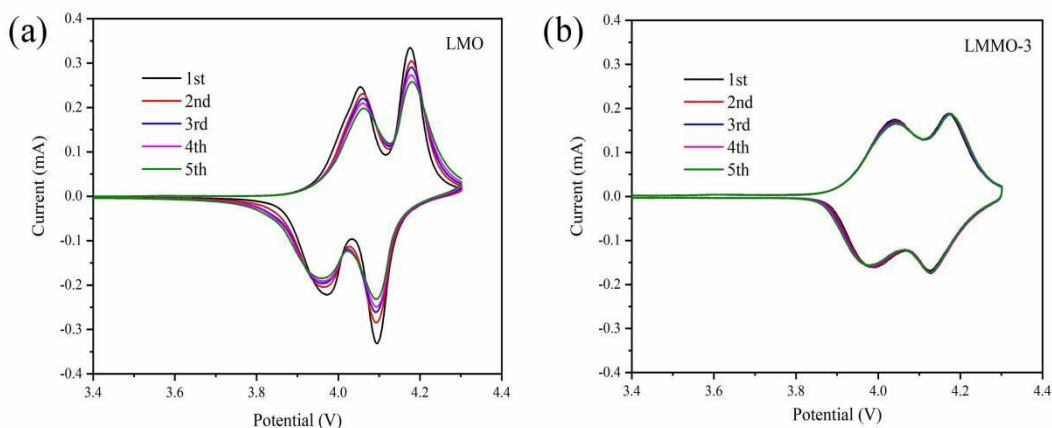


Figure 7. The CV curves of (a) LMO and (b) LMMO-3 at a scan rate of 0.05 mV s^{-1} for the initial five cycles at 25°C

Cyclic voltammetry analysis was then performed to study the kinetic process of the LMO and LMMO-3 at scan rates of $0.1\text{--}0.8 \text{ mV s}^{-1}$, with the results shown in Fig. 8. As Fig. 8a and Fig. 8b show, the peak currents of the LMMO-3 were larger, while the redox peaks potential shifted to both sides with the increase in scan rate. Meanwhile, Fig. 8c shows the relationship between the square root of the scan rate ($v^{1/2}$) and the ipa2 peak current (I_p), revealing that they had a good linear relationship and indicating that the Li-ion charge/discharge process is essentially a diffusion-control process. The Li^+ diffusion coefficient (D_{Li^+}) could be calculated using the following formula [46–48]:

$$I_p = 2.69 \times 10^5 \times n^{3/2} \times A \times D_{\text{Li}^+}^{1/2} \times C_{\text{Li}^+} \times v^{1/2}$$

where I_p is the peak current (mA), n is the electron transfer number ($n = 1$), A is the electrode surface area (cm^2), C_{Li^+} represents the Li-ion concentration ($0.02378 \text{ mol cm}^{-3}$) and v is the scan rate (mV s^{-1}). The D_{Li^+} of the LMO and the LMMO-3 were calculated to be 3.64×10^{-12} and $5.69 \times 10^{-12} \text{ cm}^2 \text{ s}^{-1}$, respectively. Clearly, the diffusion coefficient of the LMMO-3 was larger, indicating that in the charge/discharge process, the Li-ion transfer rate was rapid, meaning the rate performance was excellent. This is related to the good crystallinity and stable crystal structure of the material.

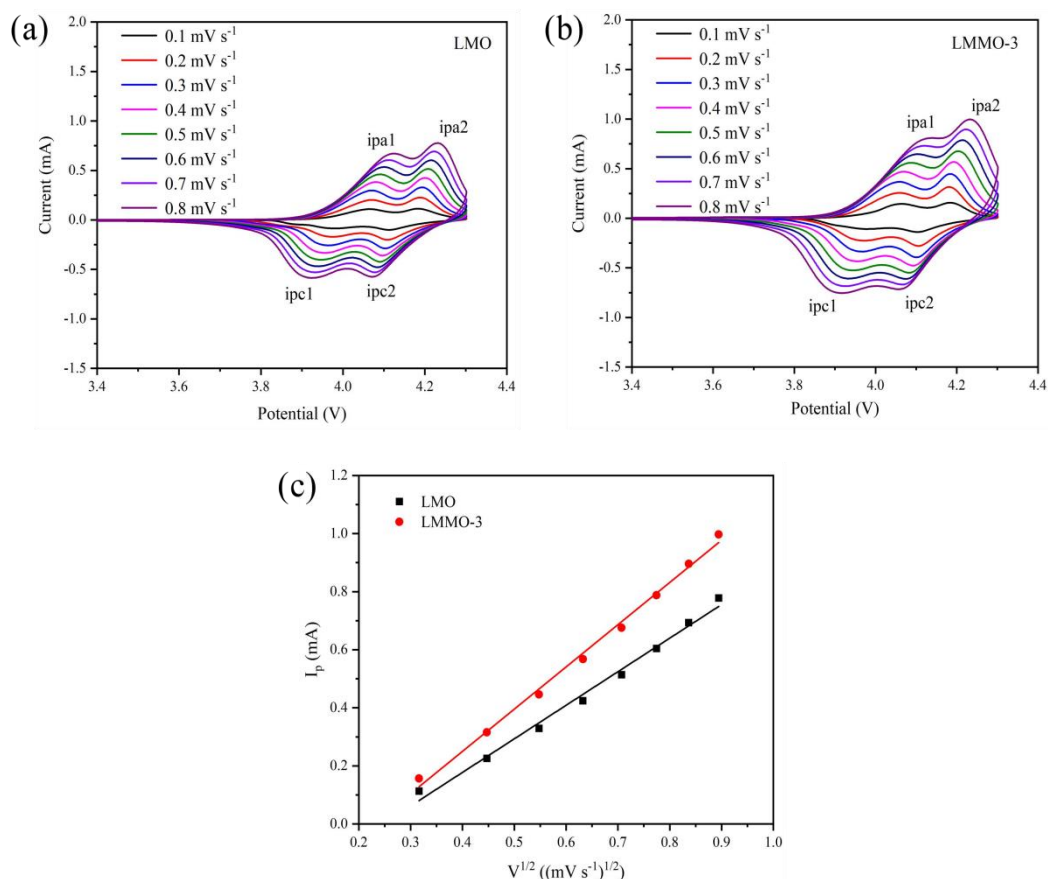


Figure 8. The CV curves of (a) LMO and (b) LMMO-3 at various scan rates at 25°C from 0.1 to 0.8 mV s^{-1} and (c) the function plots of the peak current (I_p) of ipa2 and the square root of the scan rates ($v^{1/2}$)

The EIS spectra of the LMO and LMMO-3 after the first and 100th cycles are presented in Fig. 9. The intercept of the semi-arc with the X-axis in the high frequency region indicates the solution resistance of the electrolyte (R_s), while the semi-arc in the intermediate frequency region is generated by the interaction between the interface impedance (R_f) and the charge transfer impedance (R_{ct}) that is related to the electronic conductivity of the material [49]. Meanwhile, LiMn_2O_4 is an n-type semiconductor material, and its electron conduction is mainly realised by the electron transition between low-valence Mn^{3+} and high-valence Mn^{4+} ions. In the figure, the oblique line represents the Warburg impedance (W_l), which is related to the Li^+ ions diffusion rate in the electrode. According to the principle of least-square fitting, the equivalent circuit model was established based on the experimental data, and the impedance value was fitted, as is shown in Table 3. After the first cycle, the R_f and R_{ct} values of the LMMO-3 were smaller at 46.29 and 23.91 Ω , respectively. The smaller the charge transfer resistance, the higher the electronic conductivity. Meanwhile, the R_f and R_{ct} values of the LMO were larger, which had been due to the interface reaction of smaller grains. To further assess the internal impedance changes between the doped and undoped samples, the LMO and LMMO-3 were tested following 100 cycles, with the results shown in Fig. 9b. Here, the impedance difference between the two samples was more obvious after 100 cycles, with the R_f and R_{ct} values of the LMO increasing to 323.30 and 212.60 Ω , respectively, and those of the LMMO-3 increasing to 133.20 and 102.70 Ω , respectively. The resistance

of the LMO was larger after 100 cycles because the lattice structure was severely distorted and the obstacles to Li-ion migration increased [50–51]. Meanwhile, due to the fine particle size, the more stable structure and the stable Li⁺ diffusion channel, the LMMO-3 had smaller resistance values, meaning it demonstrated better cycle and multiple-rate performances.

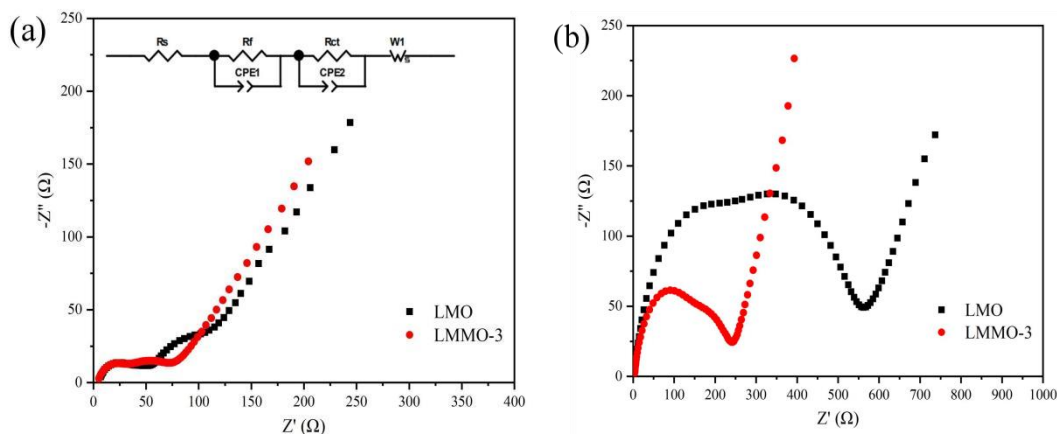


Figure 9. The EIS Nyquist plots of the LMO and LMMO-3 at room temperature: (a) after the first cycle and (b) after 100 cycles.

Table 3. Resistance fitting values based on the EIS spectra of the LMO and LMMO-3 after the first and 100th cycles

Samples	1st			100th		
	$R_s(\Omega)$	$R_f(\Omega)$	$R_{ct}(\Omega)$	$R_s(\Omega)$	$R_f(\Omega)$	$R_{ct}(\Omega)$
LMO	4.63	54.90	44.29	2.72	323.30	212.60
LMMO-3	3.99	46.29	23.91	2.90	133.20	102.70

4. CONCLUSION

In this paper, LiMg_xMn_{2-x}O₄ particles with good crystallinity were prepared via a hydrothermal method. The morphologies of the samples were octahedral or polyhedron in shape, while the crystal particles shapes of the doped material were more regular. Overall, the LiMn_{1.97}Mg_{0.03}O₄ demonstrated better cycle and rate performances at room temperature, with the first specific discharge capacity 124.3 mAh g⁻¹ at 0.2 C and the capacity retention 94.29% after 100 cycles, while its specific capacity reached 64.0 mAh g⁻¹ at 10 C. At a higher temperature (55°C), the initial specific discharge capacity of the LMMO-3 sample was 125.6 mAh g⁻¹ at 0.2 C, with a capacity retention rate of 85.43% after 100 cycles. The CV curves and the EIS spectra indicated that doping an appropriate amount of Mg²⁺ increases the Li⁺ diffusion and reduces the internal resistance during the charge/discharge process. Overall, the results demonstrated that Mg doping is beneficial for improving the electrochemical performance of spinel

LiMn₂O₄, with the partial replacement of Mn³⁺ with Mg²⁺ ions alleviating the lattice distortion and stabilising the crystal structure, meaning the cycling stability was greatly improved.

ACKNOWLEDGEMENTS

The authors sincerely acknowledge the support of the National Nature Science Foundation of China (51764007) and the Guizhou Province Graduate Research Fund (YJSCXJH[2020]033).

References

1. S. Gawusu, X. Zhang, A. Ahmed, S.A. Jamatutu, E.D. Miensah, A.A. Amadu and F.A.J. Osei, *Sustain Energy Techn.*, 52 (2022)102108.
2. M. Salanne, B. Rotenberg, K. Naoi, K. Kaneko, P.L. Taberna, C.P. Grey, B. Dunn and P. Simon, *Nat Energy*, 1 (2016)16070.
3. H. Xiao, Y. Wang, K. Xie, S. Cheng and X. Cheng, *J Alloys Compd.*, 738 (2018) 25.
4. C. Xu, J. Li, X. Feng, J. Zhao, C. Tang, B. Ji, J. Hu, C. Cao, Y. Zhu and F.K. Butt, *Electrochim. Acta*, 358 (2020)136901.
5. Z. Yang, J. Zhang, M.C. Kintner-Meyer, X. Lu, D. Choi, J.P. Lemmon and J. Liu, *Chem Rev.*, 111 (2011) 3577.
6. Z.J. Zhang, S.L. Chou, Q.F. Gu, H.K. Liu, H.J. Li, K. Ozawa and J.Z. Wang, *ACS Appl Mater Interfaces*, 6 (2014) 22155.
7. P. Albertus, S. Babinec, S. Litzelman and A. Newman, *Nat. Energy*, 3 (2017) 16.
8. L. Xiong, Y. Xu, T. Tao and J.B. Goodenough, *J. Power Sources*, 199 (2012) 214.
9. X. Li and Y. Xu, *Electrochem. Commun.*, 9 (2007) 2023.
10. Z. Cai, Y. Ma, X. Huang, X. Yan, Z. Yu, S. Zhang, G. Song, Y. Xu, C. Wen and W. Yang, *J. Energy Storage.*, 27 (2020) 101036.
11. Y. Xia, H. Takeshige, H. Noguchi and M. Yoshio, *J. Power Sources*, 56 (1995) 61.
12. Y. Qin, X. Chen, A. Tomaszewska, H. Chen, Y. Wei, H. Zhu, Y. Li, Z. Cui, J. Huang, J. Du, X. Han, L. Lu, B. Wu, K. Sun, Q. Zhang and M. Ouyang, *Cell Rep. Phys. Sci.*, 3 (2022) 100708.
13. B. Xu, D. Qian, Z. Wang and Y.S. Meng, *Mater. Sci. Eng. R.*, 73 (2012) 51.
14. L. Cai, Y. Dai, M. Nicholson, R.E. White, K. Jagannathan and G. Bhatia, *J. Power Sources*, 221 (2013) 191.
15. R.S. Ledwaba, J.C. Womack, C.K. Skylaris and P.E. Ngoepe, *Mater Today Commun.*, 27 (2021) 102380.
16. A. Yamada, M. Tanaka, K. Tanaka and K. Sekai, *J. Power Sources*, 81-82 (1999) 73.
17. H. Yamane, T. Inoue, M. Fujita and M. Sano, *J. Power Sources*, 99 (2001) 60.
18. C.Y. Ouyang, S.Q. Shi and M.S. Lei, *J Alloys Compd.*, 474 (2009) 370.
19. J.S. Kim, K. Kim, W. Cho, W.H. Shin, R. Kanno and J.W. Choi, *Nano Lett.*, 12 (2012) 6358.
20. K.Y. Chung and K.-B. Kim, *Electrochim. Acta*, 49 (2004) 3327.
21. Y. Kim, J. Lim and S. Kang, *Int. J. Quantum Chem.*, 113 (2013) 148.
22. M. Pasqualini, S. Calcaterra, F. Maroni, S.J. Rezvani, A. Di Cicco, S. Alexander, H. Rajantie, R. Tossici and F. Nobili, *Electrochim. Acta*, 258 (2017) 175.
23. Mosqueda Laffita, L.A. Tavera Carrasco and E.L. Perez-Cappe, *J. Power Sources*, 490 (2021) 229519.
24. H. Huang, C.A. Vincent and P.G. Bruce, *J. Electrochem. Soc.*, 146 (1999) 3649.
25. X. Wang, H. Nakamura and M. Yoshio, *J. Power Sources*, 110 (2002) 19.
26. S. Liu, J. Su, J. Zhao, X. Chen, C. Zhang, T. Huang and J. Wu, A. Yu, *J. Power Sources*, 393 (2018) 92.
27. Z. Wang, J. Du, Z. Li and Z. Wu, *Ceram. Int.*, 40 (2014) 3527.

28. X. Luo, M. Xiang, Y. Li, J. Guo, X. Liu, H. Bai, W. Bai and C. Su, *Vacuum*, 179 (2020) 109505.
29. Y. Idemoto, F. Tejima, N. Ishida and N. Kitamura, *J. Power Sources*, 410-411 (2019) 38.
30. X. Feng, Y. Tian, J. Zhang and L. Yin, *Powder Technol.*, 253 (2014) 35.
31. H. Song, Y. Zhao, Y. Niu, Z. Wu and H. Hou, *Solid State Ionics*, 325 (2018) 67.
32. M. Xiang, L. Ye, C. Peng, L. Zhong, H. Bai, C. Su and J. Guo, *Ceram. Int.*, 40 (2014) 10839.
33. M. Xiang, C.-W. Su, L. Feng, M. Yuan and J. Guo, *Electrochim Acta*, 125 (2014) 524.
34. G.-M. Song, W.-J. Li and Y. Zhou, *Mater. Chem. Phys.*, 87 (2004) 162.
35. Y.-S. Lee, N. Kumada and M. Yoshio, *J. Power Sources*, 96 (2001) 376.
36. H. Zhao, X. Liu, C. Cheng, Q. Li, Z. Zhang, Y. Wu, B. Chen and W. Xiong, *J. Power Sources*, 282 (2015) 118.
37. Y. Hou, K. Chang, H. Tang, B. Li, Y. Hou and Z. Chang, *Electrochim. Acta*, 319 (2019) 587.
38. C. Zhang, J. Su, T. Wang, K. Yuan, C. Chen, S. Liu, T. Huang, J. Wu, H. Lu and A. Yu, *ACS Sustain Chem Eng.*, 6 (2018) 7890.
39. W. Xu, L. He and Z. Zhao, *Desalination*, 503 (2021) 114935.
40. X. Lv, S. Chen, C. Chen, L. Liu, F. Liu and G. Qiu, *Solid State Sci*, 31 (2014) 16.
41. Z. Cai, Y. Ma, X. Huang, X. Yan, Z. Yu, S. Zhang, G. Song, Y. Xu, C. Wen and W. Yang, *J. Energy Storage*, 27 (2020) 101036.
42. B. Subramani, U.V. Varadaraju, R. Gopalan and P. Raju, *Electrochim. Acta*, 301 (2019) 342.
43. J. Guo, J. Ruan, Y. Pang, H. Sun, J. Yang and S. Zheng, *Prog Chem*, 33 (2021) 1390.
44. S. Shi, C. Ouyang, M. Lei and W. Tang, *J. Power Sources*, 171 (2007) 908.
45. K. Chudzik, M. Lis, M. Bakierska, M. Gajewska and M. Molenda, *J. Power Sources*, 434 (2019) 226725.
46. Y. Yu, M. Xiang, J. Guo, C. Su, X. Liu, H. Bai, W. Bai and K. Duan, *J Colloid Interface Sci.*, 555 (2019) 64.
47. Y. Lu, X. Luo, H. Bai, J. Guo, M. Xiang, C. Su, X. Liu, W. Bai and R. Wang, *Vacuum*, 158 (2018) 223.
48. M.A. Razmjoo Kholari, M.K. Azar, M. Esmaceli, M. Tanhaei, A. Dolati and S.M. Hosseini H, *J Alloys Compd.*, 843 (2020) 154924.
49. H. Zhao, S. Liu, Z. Wang, Y. Cai, M. Tan and X. Liu, *Electrochim. Acta*, 199 (2016) 18.
50. S. Luo, H. Guo, S. Zhang, Z. Wang, X. Li, G. Yan and J. Wang, *Ceram. Int.*, 45 (2019) 8607.
51. Y. Cai, Y. Huang, X. Wang, D. Jia and X. Tang, *Ceram. Int.*, 40 (2014) 14039.